Proceedings World Geothermal Congress 2026
Calgary, Canada, June 8 – 11, 2026

Seismicity Across the Supercritical-to-Steam Transition: Comparative Patterns Above Two Distinct Heat Sources in the Hengill Geothermal Field, Iceland

Anna Barth[1]*, Eric Beaucé[2], Vala Hjörleifsdóttir[3], Seth Saltiel[4], Tushar Mittal[5], Ben Holtzman[1,2]
Strabo Engineering[1]*, Lamont-Doherty Earth Observatory[2], Reykjavik University[3], Cornell University, Penn State University[5]
anna@straboengineering.com

Keywords: Earthquake statistics, seismic wavefield coherence, supercritical, Hengill, Nesjavellir

ABSTRACT

The seismic wavefield contains rich information about geothermal reservoir dynamics that is only beginning to be understood. The ambient wavefield, coherent noise, and seismicity all reflect the structure and processes occurring within a volume of crust. In Iceland, the geothermal resources are natural shallow hydrothermal systems, which are tapped for hot liquid and steam. Below ~ 2.5-3 km depth, the fluid becomes supercritical and the permeability structure may also change substantially. We present results from a new study of seismic data from the COSEISMIQ broadband array in the northern part of the Hengill Geothermal Area in Southwestern Iceland, with a focus on the Nesjavellir field and the adjacent but hydrologically disconnected, Mosfellsheiði area. Our workflow consists of (1) producing high-resolution micro-earthquake catalogs, (2) analyzing the temporal clustering and magnitude statistics, and (3) characterizing the coherent seismic energy sources in the ambient wavefield. We identify interesting spatial variations in the earthquake statistics both within and between the two geothermal areas and propose a link to stress state and fracture network morphology. We are able to detect coherent seismic energy in the frequency band 1-20 Hz that appears intermittently and is most frequently located within the Nesjavellir area at ~ 1-2 km depth, although it moves in depth and sometimes appears further south or in the Mosfellsheiði area.

1 INTRODUCTION

Iceland is an ideal setting for studying the dynamics of natural hydrothermal systems as superhot geothermal resources. While magnetotelluric (MT) and seismic tomography provide static images of the structure of the crust (convolving composition, temperature and damage distributions), seismicity and the seismic wavefield provide information on the dynamics of a reservoir, as fluid distribution and movement are intricately tied to the processes that cause seismicity. Advances in both seismic instrumentation and processing methods are leading to huge improvements in the resolution of pattern detection. As pattern discovery, characterization and understanding improve, there will be more information for geothermal reservoir control during operation, for optimization of permeability development and mitigation of excess seismicity.

Towards these aims, we study the Hengill area in SE Iceland, using a recent broadband seismic array database produced from the COSEISMIQ project (Obermann et al., 2022). We use two array analysis tools for high resolution seismicity detection and location (combined backprojection and matched filtering, BPMF (Beaucé et al., 2024)), and for characterization of coherent signals in continuous recording of the seismic wavefield, (CovSeisNet, Seydoux et al., 2016). We animate and sonify the high-resolution catalogs to represent these patterns in ways that we can perceive the spatial-temporal patterns (Holtzman et al., 2013; Paté et al., 2022), and then analyze the earthquake statistics using some standard and novel statistical descriptors. We identify sources of coherent seismic energy and track how this varies over time and space. We then speculate on drivers for these patterns and what they may tell us about the thermomechanical state of the rock and fluid in the two sub-regions of the northern Hengill area.

We focus on the northern section to compare patterns in the Nesjavellir and Mosfellsheiði regions. It has been suggested that these two reservoirs both have heat sources at depths of ~ 4-6 km (Napolitano et al., 2025; Amoroso et al., 2022), but there are several differences: Nesjavellir has a well-developed surface expression of faulting associated with rifting and volcanism (last erupting 2000 years ago), as well as geothermal surface manifestations, and is an actively exploited geothermal reservoir. In contrast, Mossfellsheiði has a less pronounced/mature fault system at the surface, has been volcanically quiet far longer, has no surface expression of its geothermal reservoir, and has not yet been drilled for geothermal resources. In other words,

they differ in their shallow tectonic-geothermal structure and their perturbation by human activity (tapped and un-tapped).

Comparative analysis of these two sites, along with the previously and newly observed patterns in seismicity lead us to the following questions:

- How does seismicity change as a function of the state of the reservoir fluid, from supercritical fluid to liquid to steam?
- How does geothermal extraction of mass and heat affect the stress state and fracture network morphology of the reservoir, as inferred from the earthquake statistics?

1.1 Northern Hengill Geothermal Area (Nesjavellir and Mosfellsheiði)

The geothermal areas surrounding the Hengill volcano host the two largest power plants in Iceland. Supercritical fluids have been found at Nesjavellir, a power plant to the north of the volcano, and this area is the proposed site for the IDDP-3 drilling project (Pálsdóttir et al., 2025). From November 2018 to August 2021, a permanent seismic network was complemented with 23 seismic stations in the Hengill area. Many geophysical studies have characterized the seismicity and structure around Nesjavellir. Coinciding with the location of the last fissure eruption at Hengill 2ka, a region of high Vp/Vs ratios (Amoroso et al., 2022), strong seismic attenuation (Napolitano et al., 2025) and high electrical conductivity (Vilhjálmsson et al., 2019) has been interpreted as magmatic intrusions which provide the heat source for the geothermal field above. This is also the location of deep seismicity, which is largely confined to a NNE-striking plane that dips west. Shallow seismicity is more diffuse and is thought to be related to geothermal extraction (Obermann et al., 2022). Significant seismic activity was observed in the summer of 2021, clustering at Mosfellsheiði, just west of Nesjavellir, in an area which has no deep boreholes. Similar to Nesjavellir, there is a region at 4-6 km depth with high Vp/Vs ratios (Amoroso et al., 2022), strong seismic attenuation (Napolitano et al., 2025) and high electrical conductivity (Árnason et al., 2010). The seismicity appears to follow the boundary of this region. Nesjavellir and Mosfellsheiði provide a natural comparative case study to understand the relationship between geothermal power generation and seismicity.

2 METHODS

2.1 Earthquake Detection and Location

To study how the earthquake statistics vary both between and within Mosfellsheiði and Nesjavellir, we need a high number of events, extending down to low magnitudes, even those below the noise level. To this end, we used BPMF, a backprojection and matched filtering workflow (Beaucé et al., 2024), to detect and locate seismicity in the Hengill region. This method consists of two main stages: first, a machine-learning-enhanced backprojection technique (PhaseNet, Zhu and Beroza, 2019) is used to detect events from continuous seismic data from a network of stations (fig. 1). The backprojection locations were refined using the NonLinLoc software (Lomax et al., 2000, 2014) on the phase picks from PhaseNet. Well-located events were then used as templates for a matched-filter approach to detect small events missed in the first stage. We used a detection threshold of eight times the running standard deviation of the network-averaged correlation coefficients. The newly detected events were individually located if PhaseNet could produce more than three pairs of P- and S-wave picks; otherwise, they were given their template's location. For large enough events, magnitude was determined by fitting the Boatwright model to the S-wave displacement spectrum (Boatwright, 1978). When poor signal to noise (typically for small events) prevented this approach, we calculated an approximate moment magnitude M_{w*}, following the method outlined in Beaucé et al. (2025).

2.2 Earthquake Statistics

The collective properties of earthquakes result from the physics of earthquakes and earthquake interactions as well as from the physical characteristics of the system of faults that host those earthquakes. We analyzed the temporal and size statistics of the detected events. We estimated all statistical parameters described below in overlapping subsets of our earthquake catalog corresponding to groups of closely located templates (less than 0.5 km).

2.2.1 Temporal Statistics

Earthquake occurrence follows highly non-Poissonian temporal statistics, reflecting the non-linear dynamics of crustal processes. The rate of seismicity exhibits strong local heterogeneities with variations across a wide range of temporal scales. Characterizing these variations help us understand fault properties. Here, we measured and

characterized the occupation probability, $\Phi(\tau)$, of seismic sequences, which is the probability that any given interval of duration τ is occupied by one earthquake or more (Smalley Jr et al., 1987; Beaucé, 2025). We used a three-parameter empirical model to describe Φ (Beaucé, 2025):

$$\Phi(\tau\,;\, n\, =\, 1\, -\, D_\tau\,, \tau_c, \alpha) = \frac{1}{\left(1 + \left(\frac{\tau_c}{\tau}\right)^{n\alpha}\right)^{1/\alpha}} \quad (1)$$

The model parameters are: the intermittency parameter α, which describes whether seismicity is continuous ($\alpha \lesssim 1$) or, instead, organized into bursts spaced by quiet periods ($\alpha \gtrsim 2$, higher values implying more regular bursts), the temporal fractal dimension D_τ ($0 \leq D_\tau \leq 1$), which characterizes the strength and topology of the bursts, and the intermittency time scale τ_c, which gives the typical interburst time. Note that in the following discussion and figures, we use the normalised interburst time, $\theta_c = \lambda\tau_c$, where λ is the average earthquake rate. Thus, D_τ quantifies the tendency for earthquakes to form temporal cascades, and higher values of D_τ imply that a larger fraction of events concentrates into the bursts. Note that $\Phi(\tau)$ is closely related to the interevent time distribution but presents several practical benefits, in particular for the analysis of matched-filtering catalogs (more details in Beaucé, 2025).

2.2.2 Earthquake Size Distribution

Earthquake sizes are commonly measured on a magnitude scale, M, and magnitudes are typically exponentially distributed, according to the Gutenberg-Richter law (Gutenberg and Richter, 1941):

$$log_{10}N(M' \geq M) = a - bM \quad (2)$$

If M is related to the seismic moment M_0 through a relationship $M = \beta + \alpha\, log_{10}M_0$, such as the moment magnitude $M_w = 2/3(log_{10}M_0 - 9.1)$ (Hanks and Kanamori, 1979), then the Gutenberg-Richter law expresses a power-law distribution of seismic moments with exponent $-2b/3$. The b-value is often related to the spatial fractal dimension of earthquakes and size distribution or roughness of faults (higher b-value indicating higher spatial fractal dimension and rough faults Goebel et al., 2017) or to differential stress (lower b-value meaning higher stress, Scholz, 2015).

Variations in the Gutenberg-Richter b-value are physically significant when they can be interpreted as variations in the exponent of the power-law distribution of seismic moments. Thus, we use the approximation of the moment magnitude for small events, M_{w*}, described in Beaucé et al. (2025). We estimated the magnitude of completeness with the maximum curvature method (Wiemer and Katsumata, 1999) and used the maximum likelihood estimate of the b-value (Aki, 1965).

2.3 Broadband Wavefield Coherence Analysis>

Important information about crustal systems may be obtained from non-conventional seismic signals, like, for example, in the case of tremor activity (Seydoux et al., 2016; Caudron et al., 2022; Soubestre et al., 2025). These signals are emergent, eluding conventional earthquake detectors, but exhibit spatiotemporal coherence. We thus tracked the coherence of the seismic wavefield across our seven-station array by applying the CovSeisNet algorithm of Seydoux et al. (2016). Continuous waveform streams from each station were first preprocessed by normalizing by the envelope and whitening the amplitude spectrum. We then segmented the streams into 100 sec windows and computed the Fourier transform for each window. Averaging the cross-spectra matrices for twenty 50%-overlapping windows gives the covariance matrix. These window parameters were chosen to enhance the contribution of continuous signals (i.e., tremor) rather than discrete events, to provide complementary information to the earthquake part of this study. We performed eigendecomposition on each covariance matrix to determine its eigenvalues, the distribution of which can provide an estimate of the number of independent sources shaping the wavefield (Seydoux et al., 2016). We quantified this behaviour using the Shannon diversity, defined as the exponential of the entropy of the eigenvalue distribution. The 'diversity' ranges from one to the number of seismic stations in the array, with larger values indicating a greater number of independent sources.

To locate the source of any coherent seismic energy, we use backprojection on the station-pairwise cross-correlation functions, with the differential travel times calculated already during the earthquake catalog creation. We bandpass-filtered the cross-correlation functions between 0.1-1 Hz and 1-20 Hz and calculated their max-normalized envelope before backprojection. We thus obtained two locations for each set of cross-correlations, one for sources radiating coherent waves at low frequencies (0.1-1 Hz, most likely oceanic noise) and one for high frequencies (1-20 Hz, the local sources we are interested in).

3 RESULTS

3.1 Earthquake Catalog

Figure 1 shows the earthquake catalog, with 38771 events ranging from M_{w*} -0.27 to M_{w*} 3.75. The seismicity occurs in well-defined spatial clusters, similar to those found by Obermann et al. (2022). We focus on the northern clusters of Mosfellsheiði, the unharnessed but seismically active area to the NW, and Nesjavellir, one of the largest power plants in Iceland. In both regions there is a cluster of deep seismicity ~ 2.5-5 km depth. Nesjavellir also hosts a distinct shallow cluster from ~ 0.5-2.5 km, while we did not detect any significant shallow seismicity at Mosfellsheiði.

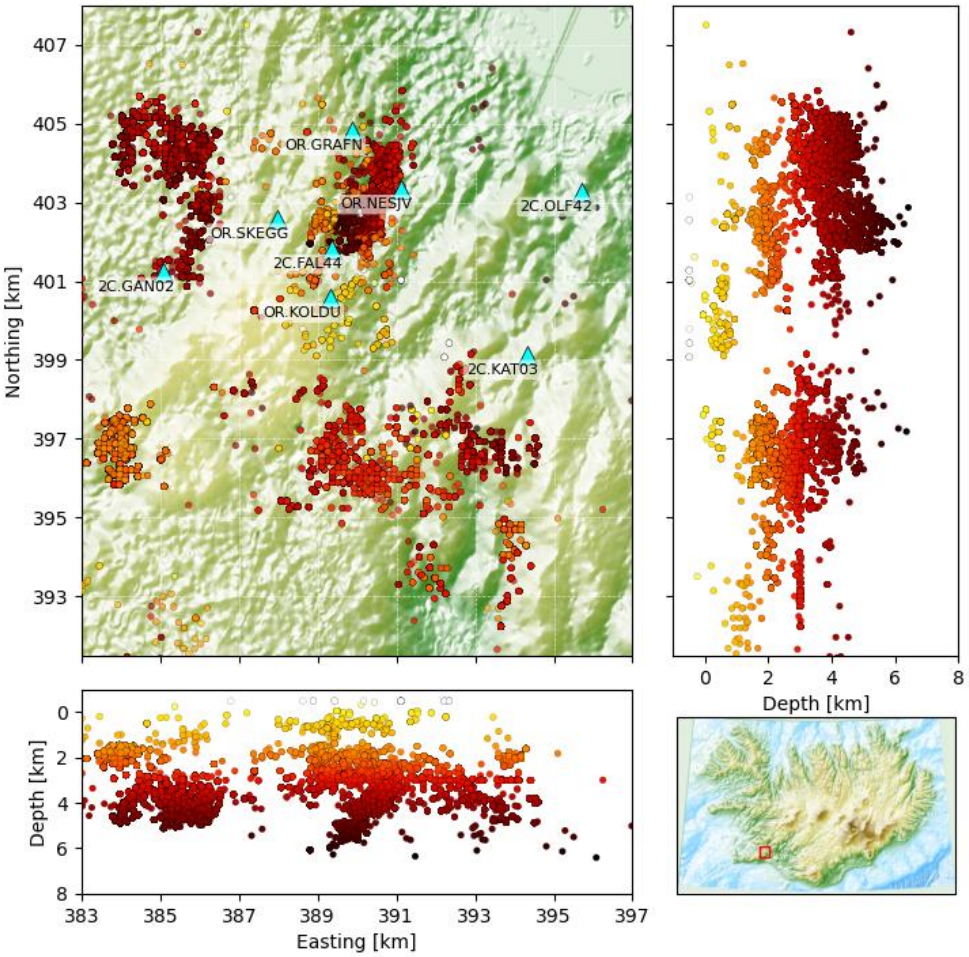


Figure 1. Overview map and E-W, N-S cross sections of earthquake catalog with color representing depth. Seismic stations used from COSEISMIC and ISOR/ON networks shown in blue triangles.

Looking at the catalog over time (fig. 2) reveals that both regions are dominated by bursts of activity, although Nesjavellir has a higher rate of seismicity between bursts. Within Nesjavellir, the shallow cluster has longer return times on average and is less active during the bursts.

3.2 Earthquake Statistics

Observed differences between shallow and deep seismicity at Nesjavellir translate into low, $D_\tau \approx 0.1$, and moderate-to-high fractal dimensions, $D_\tau \approx 0.2$-0.3, respectively (fig. 4e). The shallow and deep seismicity dichotomy outlined by the temporal statistics is reinforced by clear variations in the earthquake size distributions, with b-values $b \approx 1$ near the surface and higher b-values $b \approx 1.2{-}1.4$ deeper than 3 km (fig. 4h). The intermittency parameter, α, shows relatively uniform values $\alpha \approx 1.5{-}2$. Most variability in Mosfellsheiði occurs along the NW-SE direction. NW seismicity exhibits high fractal dimensions $D_\tau \approx 0.3$ and with b-values $b \approx 1.2{-}1.4$ whereas SE seismicity shows $D_\tau \approx 0.1$ and includes a large fraction of $b \approx 0.8$ b-values. The intermittency parameter, α, shows relatively uniform values $\alpha \approx 1$. The significantly larger fraction of locations with high fractal dimensions in Mosfellsheiði, compared to Nesjavellir, and the longer normalized inter-burst times θ_c emphasize the overall stronger tendency for Mosfellsheiði earthquakes to occur in bursts. Lower α values at Mosfellsheiði reflect the wider range of inter-burst times.

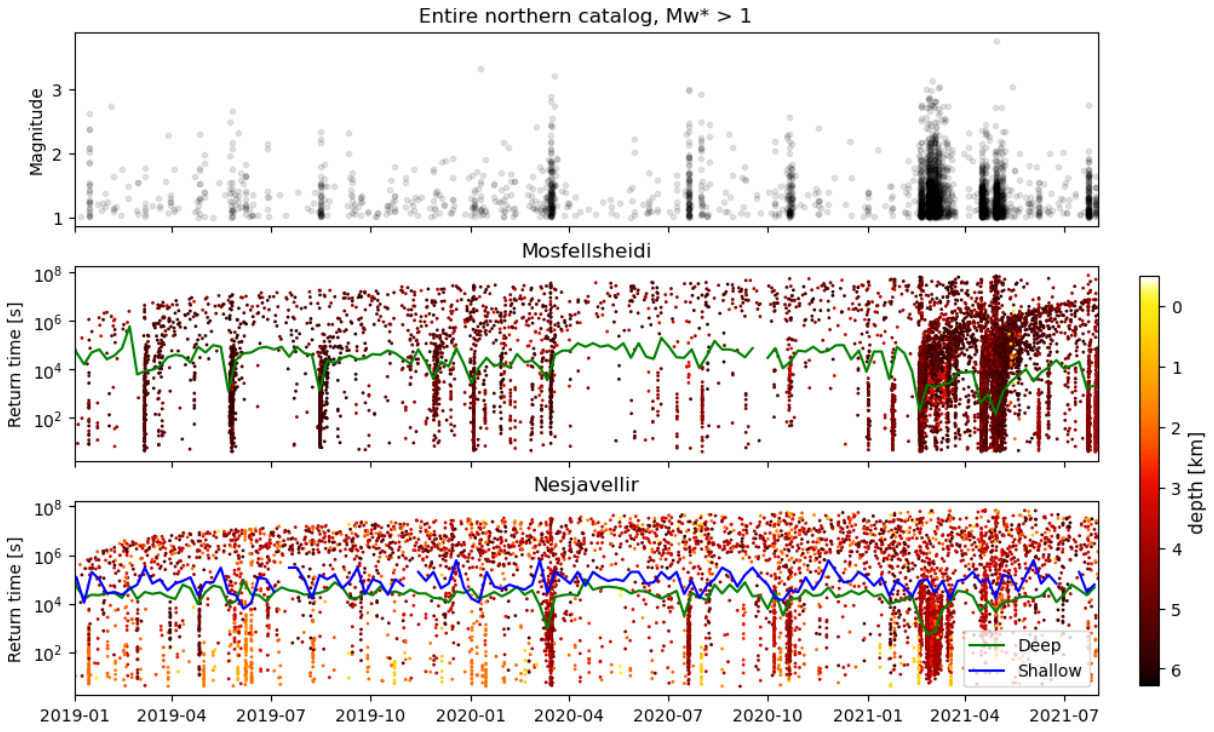


Figure 2: Approximate moment magnitude and return time over 2.5 years for earthquakes in the northern region (Mosfellsheiði and Nesjavellir). Earthquake swarms appear as vertical stripes. The inverse of the weekly average number of events shown in green for Mosfellsheiði and deep Nesjavellir (>2.8 km) and blue for shallow Nesjavellir (<2.8 km).

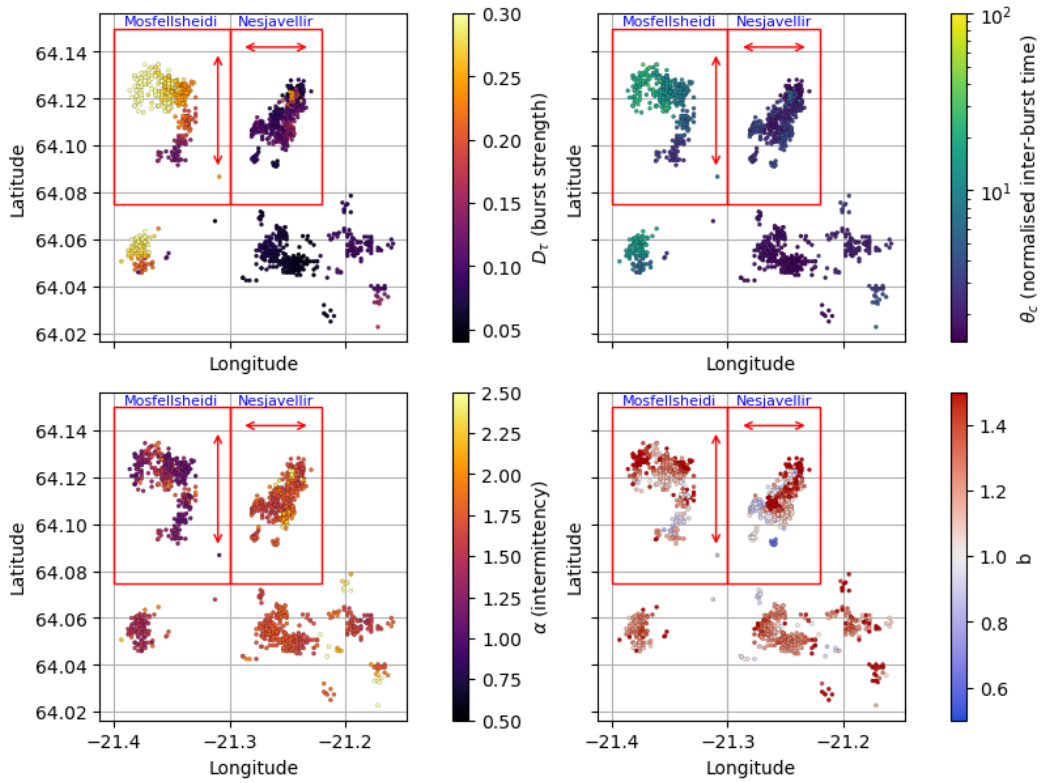


Figure 3: Map view of results from statistical analysis. Events from templates within 0.5 km are used to calculate the parameters ($D_\tau, \alpha, \theta_c, b$) for each template. Each point represents the parameter for that template (n=1510). Red boxes and arrows show focus regions and cross-section directions for fig. 4.

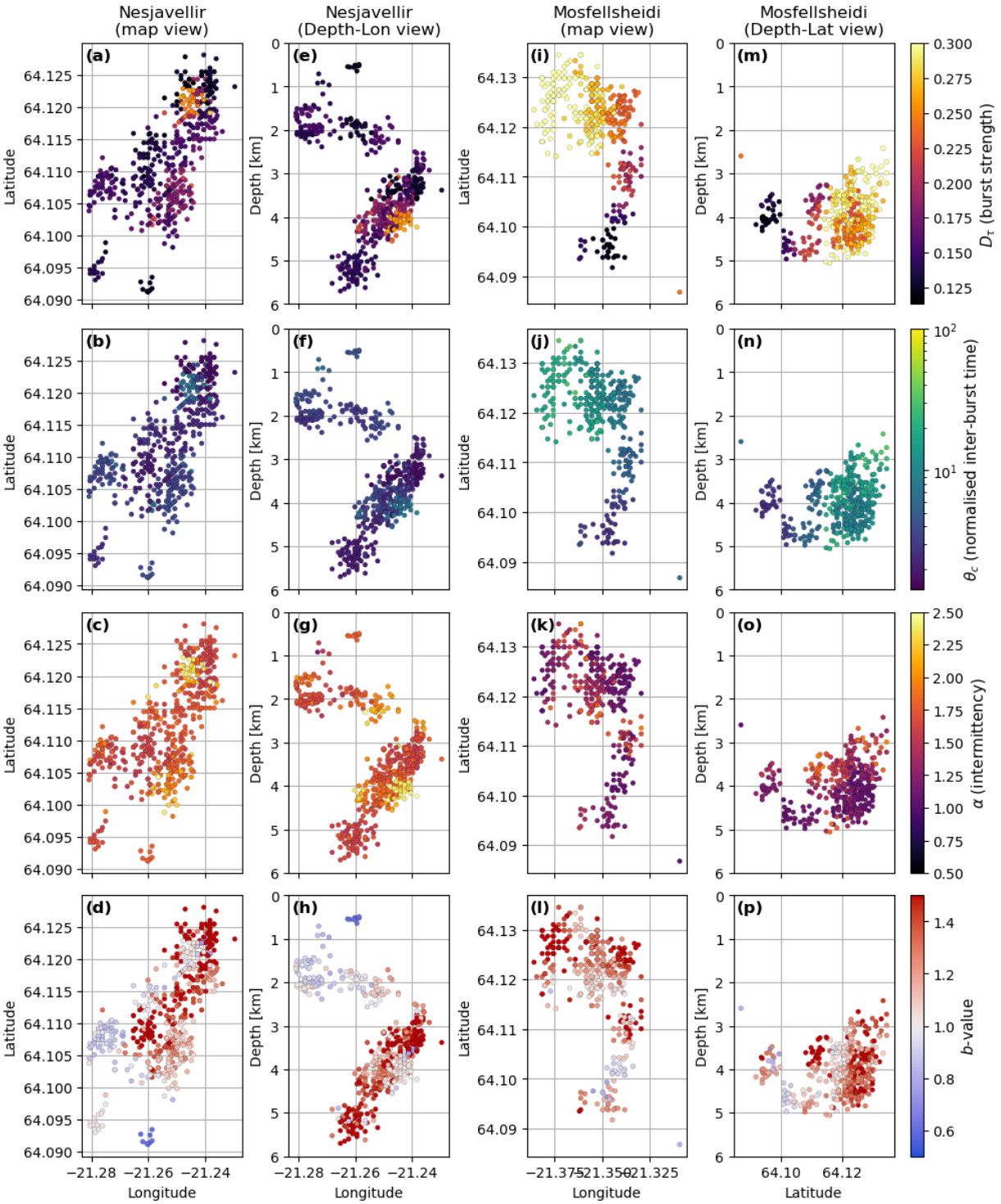


Figure 4: Zoom in map view and depth section of statistical parameters for Mosfellsheiði and Nesjavellir.

3.3 Wavefield Coherence Imaging

An example 3-day section of the coherence array is shown in fig. 5. Bright colours indicate a coherent, localised source of seismic "noise". The bright band at 0.1-1 Hz is dominated by the ocean microseism, and the bright transient signals at <0.1 Hz come from teleseismic events. Horizontal streaks observed at high frequencies (1-20 Hz), particularly visible on the morning of March 16th 2020, reveal sources at discrete frequencies active over a finite period of time likely related to geothermal extraction operations. The vertical stripes indicate the sustained occurrence of small local earthquakes within the 100-sec window used for covariance computation.

The backprojection locations (fig. 5, bottom panels) add constraints on the sources shaping the observed time-frequency coherency (see Discussion). The 0.1-1.0Hz backprojection yields consistent out-of-network locations toward the southeast, emphasizing the microseismism origin of the 0.1-1.0Hz signal.

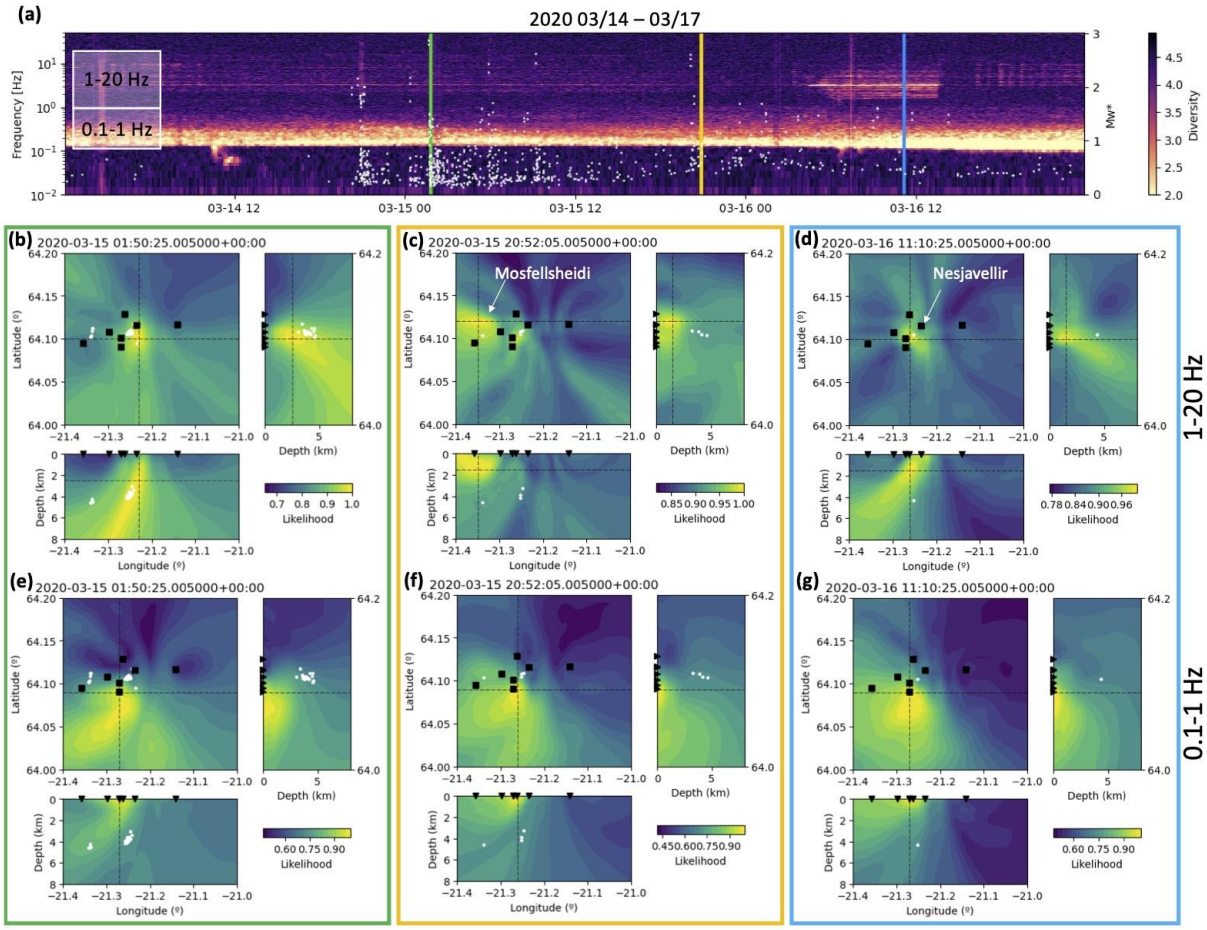


Figure 5: (a) coherence array for example 3-day period showing signals from oceanic microseism, teleseismic earthquakes, local earthquakes, and intermittent 1-20 Hz noise. Mw* from earthquake catalog is overlain (white dots). Below: location of noise source for frequency bands 1-20 Hz (b,c,d) and 0.1-1 Hz (e,f,g) for three different times highlighted in panel (a).

4 DISCUSSION AND CONCLUSIONS

Our machine-learning- and matched-filtering-enhanced earthquake catalog offers new insights into the rich seismic activity at Nesjavellir and Mosfellsheiði, allowing us to better understand their mechanics and the relationships between these two groups. Strongly time clustered seismicity (high D_τ) is caused by strong earthquake interactions (static and dynamic stress transfers, creep bursts, pore-fluid pressure perturbations, viscous relaxation, etc, Burridge and Knopoff, 1967; Gomberg et al., 1997; Hardebeck et al., 1998; Dublanchet et al., 2013; Miller, 2020; Beaucé, 2025) whereas weakly time clustered seismicity is symptomatic of a system dissipating energy aseismically (Lohman and McGuire, 2007). The b-value provides information on stress and fault network topology, with higher b-values presumably associated with lower stress environments (Scholz, 2015) and highly ramified fault network or rough faults (Aki, 1981; Goebel et al., 2017).

Seismicity at Nesjavellir clearly outlines three distinct subsystems including the seismically active shallow (1-2.5 km depth) and deep (3.0-6.0 km depth) regions and the seismically quiet transition zone in-between (Figure 4). The top of the shallow seismicity seems to coincide with the bottom of the injection wells (Amoroso et al., 2022). Our analysis of wavefield coherence suggests that production-related activity generates a source of seismic waves located around 2 km depth (Figure 5a,d), underlining the likely causal relationship between heat mining and shallow seismicity. The deep seismicity exhibits two modes (Figure 4a,e,d,h): 1) strongly time clustered ($D_\tau \approx 0.2{-}0.3$) and moderate b-value seismicity ($b \approx 1.0$) surrounded by 2) weakly time clustered ($D_\tau \approx 0.1$) and high b-value ($b \approx 1.2{-}1.4$) seismicity. Moderate b-value and strong clustering indicate localized and cascading brittle deformation whereas high b-value and weak clustering is reminiscent of thermally driven seismicity taking place in a diffuse fault network (Zaliapin and Ben-Zion, 2016; Holtzman et al., 2025). Thus, we speculate that localized brittle deformation coincides with the main pathways of supercritical fluids and the surrounding high b-value seismicity outlines the highly ramified fault network characteristic of the transition

toward more ductile deformation mechanisms (Meyer et al., 2024). The seismically quieter section at 2.5-3.0 km depth would then correspond to the phase transition from supercritical fluid to steam, the steam domain spanning above 2.5 km. Fluids being at the core of the dynamics of crustal deformation at Nesjavellir, the burst-like seismicity suggests that fluid flow is hardly continuous but, instead, shares a similar intermittency, which could be caused by cycles of pore-fluid pressure build-up and release (e.g., Farge et al., 2021). The phase change to steam and the high-permeability shallow layer may act as a mechanical buffer such that the production data does not show episodicity from deeper processes. However, future drilling and production under supercritical conditions may encounter and need to understand/manage this episodicity.

Seismicity at Mosfellsheiði is mostly restricted to 3-5 km depth and shows strongest variations laterally, from SE to NW. Unlike Nesjavellir, the b-value is well correlated with the fractal dimension, D_τ. We speculate that the increasing b-value toward NW reflects the growing immaturity of the fault systems (Goebel et al., 2017; Beaucé et al., 2025), with many yet-to-coalesce faults and fractures, restricting brittle deformation to occur as cascades of slip events across many small surfaces, explaining the strong temporal clustering (Dublanchet et al., 2013). Despite its spatial separation with Nesjavellir of approximately 5-10 km, bursts of seismicity at Mosfellsheiði seem correlated, to some extent, with those of Nesjavellir (see Figure 2 and our animated catalog). Because seismicity in high geothermal gradient areas is particularly sensitive to external stress perturbations (Hill et al., 1993; Brodsky and van der Elst, 2014; Wang et al., 2022), this synchronicity may be due to dynamic triggering. Nevertheless, more work must be done in order to elucidate whether interactions alone shape the Mosfellsheiði-Nesjavellir correlation or whether a common mechanism drives their dynamics.

Completing our analysis of the seismic wavefield beyond our investigation of statistical properties of small magnitude seismicity by systematically applying the broadband wavefield coherence analysis described in Section 2.3 will help us further address the questions and hypotheses mentioned above. Key questions to elucidate include the relationship between fluid flow and the bursts of seismicity, the influence of external stresses or magmatic processes on the dynamics of the reservoir, and the possible relationship between Nesjavellir and Mosfellsheiði.

Acknowledgements

We acknowledge support from the "Science Foundations for the Energy Earthshots" grant DE-SC0024937 to the MARBLE-C project, PI S. Saltiel (Cornell Univ., sub-award to A. Barth, Strabo Engineering). BH, EB and AB have financial interest in Strabo Engineering Inc.

REFERENCES

Aki, K. (1965). Maximum likelihood estimate of b in the formula log N= a-bM and its confidence limits. Bull. Earthquake Res. Inst., Tokyo Univ., 43:237–239.

Aki, K. (1981). A probabilistic synthesis of precursory phenomena. Earthquake prediction: an international review, 4:566–574.

Amoroso, O., Napolitano, F., Hersir, G. P., Agustsdottir, T., Convertito, V., De Matteis, R., Gunnarsdóttir, S. H., Hjörleifsdóttir, V., and Capuano, P. (2022). 3d seismic imaging of the nesjavellir geothermal field, sw-iceland. Frontiers in Earth Science, 10:994280.

Árnason, K., Eysteinsson, H., and Hersir, G. P. (2010). Joint 1d inversion of tem and mt data and 3d inversion of mt data in the hengill area, sw iceland. Geothermics, 39(1):13–34.

Beaucé, E. (2025). Measuring and modelling the occupation probability to characterize the temporal statistics of seismic sequences. Geophysical Journal International, page ggaf433.

Beaucé, E., Frank, W. B., Seydoux, L., Poli, P., Groebner, N., van der Hilst, R. D., and Campillo, M. (2024). BPMF: A backprojection and matched-filtering workflow for automated earthquake detection and location. Seismological Research Letters, 95(2A):1030–1042.

Beaucé, E., Waldhauser, F., Schaff, D., Kim, W.-Y., and Kolawole, F. (2025). The 5 April 2024 M_w 4.8 Tewksbury, New Jersey Aftershock Sequence Resolved With Machine-Learning-Enhanced Detection Methods. Geophysical Research Letters, 52(12):e2024GL113598.

Boatwright, J. (1978). Detailed spectral analysis of two small New York State earthquakes. Bulletin of the Seismological Society of America, 68(4):1117–1131.

Brodsky, E. E. and van der Elst, N. J. (2014). The uses of dynamic earthquake triggering. Annual Review of Earth and Planetary Sciences, 42(1):317–339.

Burridge, R. and Knopoff, L. (1967). Model and theoretical seismicity. Bulletin of the seismological society of america, 57(3):341–371.

Caudron, C., Soubestre, J., Lecocq, T., White, R. S., Brandsdóttir, B., and Krischer, L. (2022). Insights into the dynamics of the 2010 eyjafjallajökull eruption using seismic interferometry and network covariance matrix analyses. Earth and Planetary Science Letters, 585:117502.

Dublanchet, P., Bernard, P., and Favreau, P. (2013). Interactions and triggering in a 3-D rate-and-state asperity model. Journal of Geophysical Research: Solid Earth, 118(5):2225–2245.

Farge, G., Jaupart, C., and Shapiro, N. M. (2021). Episodicity and migration of low frequency earthquakes modeled with fast fluid pressure transients in the permeable subduction interface. Journal of Geophysical Research: Solid Earth, 126(9):e2021JB021894.

Goebel, T. H., Kwiatek, G., Becker, T. W., Brodsky, E. E., and Dresen, G. (2017). What allows seismic events to grow big?: Insights from b-value and fault roughness analysis in laboratory stick-slip experiments. Geology, 45(9):815–818.

Gomberg, J., Blanpied, M. L., and Beeler, N. (1997). Transient triggering of near and distant earthquakes. Bulletin of the Seismological Society of America, 87(2):294–309.

Gutenberg, B. and Richter, C. (1941). Seismicity of the Earth, volume 34. Geological Society of America.

Hanks, T. C. and Kanamori, H. (1979). A moment magnitude scale. Journal of Geophysical Research: Solid Earth, 84(B5):2348–2350.

Hardebeck, J. L., Nazareth, J. J., and Hauksson, E. (1998). The static stress change triggering model: Constraints from two southern California aftershock sequences. Journal of Geophysical Research: Solid Earth, 103(B10):24427–24437.

Hill, D. P., Reasenberg, P., Michael, A., Arabaz, W., Beroza, G., Brumbaugh, D., Brune, J., Castro, R., Davis, S., dePolo, D., et al. (1993). Seismicity remotely triggered by the magnitude 7.3 Landers, California, earthquake. Science, 260(5114):1617–1623.

Holtzman, B., Candler, J., Turk, M., and Peter, D. (2013). Seismic sound lab: Sights, sounds and perception of the earth as an acoustic space. In International Symposium on Computer Music Multidisciplinary Research, pages 161–174. Springer.

Holtzman, B. K., O'Ghaffari, H., Beaucé, E., Mittal, T., Barth, A., Mok, U., and Pec, M. (2025). Towards Multi-scale Coupled Thermo-Hydro-Mechanical Constitutive Models: Experiments on Thermal Cracking Under Stress with Near-field Acoustic Data. Stanford Geothermal Program.

Lohman, R. B. and McGuire, J. J. (2007). Earthquake swarms driven by aseismic creep in the Salton Trough, California. Journal of Geophysical Research: Solid Earth, 112(B4).

Lomax, A., Michelini, A., and Curtis, A. (2014). Earthquake location, direct, global-search methods. In Encyclopedia of complexity and systems science, pages 1–33. Springer.

Lomax, A., Virieux, J., Volant, P., and Berge-Thierry, C. (2000). Probabilistic earthquake location in 3D and layered models: Introduction of a Metropolis-Gibbs method and comparison with linear locations. In Advances in seismic event location, pages 101–134. Springer.

Meyer, G. G., Shahin, G., Cordonnier, B., and Violay, M. (2024). Permeability partitioning through the brittle-to-ductile transition and its implications for supercritical geothermal reservoirs. Nature Communications, 15(1):7753.

Miller, S. A. (2020). Aftershocks are fluid-driven and decay rates controlled by permeability dynamics. Nature communications, 11(1):5787.

Napolitano, F., De Siena, L., Amoroso, O., Ágústsdóttir, T., Benediktsdóttir, Á., Palo, M., Hjörleifsdóttir, V., and Capuano, P. (2025). Scattering and absorption imaging of the hengill high temperature geothermal area, southwest iceland. Journal of Geophysical Research: Solid Earth, 130(5):e2024JB030731.

Obermann, A., Wu, S.-M., Ágústsdóttir, T., Duran, A., Diehl, T., Sánchez-Pastor, P., Kristjansdóttir, S., Hjörleifsdóttir, V., Wiemer, S., and Hersir, G. P. (2022). Seismicity and 3-d body-wave velocity models across the hengill geothermal area, sw iceland. Frontiers in Earth Science, 10:969836.

Pálsdóttir, A., Sigurðsson, P., Friðriksson, Þ., Di Rienzo, D. I., and Benediktsdóttir, Á. (2025). White paper on orkuveitan‘s deep utilization plans. In PROCEEDINGS, 50t h Workshop on Geothermal Reservoir Engineering Stanford University. Stanford, California.

Paté, A., Farge, G., Holtzman, B. K., Barth, A. C., Poli, P., Boschi, L., and Karlstrom, L. (2022). Combining audio and visual displays to highlight temporal and spatial seismic patterns. Journal on Multimodal User Interfaces, 16(1):125–142.

Scholz, C. H. (2015). On the stress dependence of the earthquake b value. Geophysical Research Letters, 42(5):1399–1402.

Seydoux, L., Shapiro, N. M., de Rosny, J., Brenguier, F., and Landès, M. (2016). Detecting seismic activity with a covariance matrix analysis of data recorded on seismic arrays. Geophysical Journal International, 204(3):1430–1442.

Smalley Jr, R. F., Chatelain, J.-L., Turcotte, D. L., and Prévot, R. (1987). A fractal approach to the clustering of earthquakes: applications to the seismicity of the New Hebrides. Bulletin of the Seismological Society of America, 77(4):1368–1381.

Soubestre, J., Caudron, C., Melnik, O., Lecocq, T., Jaupart, C., Shapiro, N. M., Journeau, C., Çubuk-Sabuncu, Y., and Jónsdóttir, K. (2025). Dynamics of the 2021 fagradalsfjall eruption (iceland) revealed by volcanic tremor patterns. Journal of Geophysical Research: Solid Earth, 130(2):e2024JB029380.

Vilhjálmsson, A., Benediktsdóttir, Á., and Árnason, K. (2019). Nesjavellir og Þverárdalur einvíð túlkun viðnámsgagna og þrívíð fyrir nesjavallasvæðið. ísor report. Technical report, ÍSOR report.

Wang, W., Shearer, P. M., Vidale, J. E., Xu, X., Trugman, D. T., and Fialko, Y. (2022). Tidal modulation of seismicity at the Coso geothermal field. Earth and Planetary Science Letters, 579:117335.

Wiemer, S. and Katsumata, K. (1999). Spatial variability of seismicity parameters in aftershock zones. Journal of Geophysical Research: Solid Earth, 104(B6):13135–13151.

Zaliapin, I. and Ben-Zion, Y. (2016). A global classification and characterization of earthquake clusters. Geophysical Journal International, 207(1):608–634.

Zhu, W. and Beroza, G. C. (2019). Phasenet: a deep-neural-network-based seismic arrival-time picking method. Geophysical Journal International, 216(1):261–273.